PCCP

PAPER

View Article Online
View Journal | View Issue

Cite this: *Phys. Chem. Chem. Phys.*, 2015, **17**, 22015

$CH_3NH_3PbI_{3-x}Cl_x$ films with coverage approaching 100% and with highly oriented crystal domains for reproducible and efficient planar heterojunction perovskite solar cells†

Like Huang, Ziyang Hu,* Guoqiang Yue, Jinwang Liu, Xiaohong Cui, Jing Zhang and Yuejin Zhu*

Received 7th July 2015,
Accepted 15th July 2015

DOI: 10.1039/c5cp03934g

www.rsc.org/pccp

Depositing pinhole-free perovskite films is of vital importance for achieving high performance perovskite solar cells, especially in a planar heterojunction device. Here, perovskite films with coverage approaching 100% and with highly oriented crystal domains were obtained by carefully controlling the annealing temperature and duration. Perovskite solar cells with an average efficiency of 12% and a maximum efficiency of 15.17% were achieved in a planar heterojunction structure. Comprehensive characterization and analysis showed that appropriate annealing temperature and duration allowed the perovskite crystals to grow slowly, resulting in highly oriented crystal domains without any internal voids or pinholes. The anisotropic transport properties of perovskite crystals ensure efficient electron and hole transport to their corresponding electrodes.

Introduction

Organometal trihalide perovskites ($CH_3NH_3PbX_3$, X = Cl, Br, I, and their mixed-halide perovskites $CH_3NH_3PbI_{3-x}Cl_x$) with perfect semiconducting properties[1,2] have emerged as a new generation of solution processable, low cost materials for mesoscopic or planar heterojunction (PH) solar cells and exhibited record-breaking efficiencies.[3–7] Perovskite films can be deposited easily onto the substrates *via* single or two-step reactions of precursors.[3,5,6] Originally, metal oxides involving TiO_2 or Al_2O_3 were adopted as scaffolds to form perovskite films in mesoporous photovoltaic devices.[3–6] Later, PH architectures without mesoporous layers have been proposed to simplify the device architectures and processing procedures. Soon, high efficiencies have been reported, which demonstrates that a mesoporous layer is not necessary to achieve highly efficient perovskite solar cells (PVK SCs).[7,8] At the same time, photo-physical studies have proven that perovskite materials exhibit a carrier lifetime of several tens of nanoseconds and a diffusion length of a few hundred nanometers, confirming the validity of using a PH structure.[1,2] In addition, the intrinsic bipolar transport properties of perovskite materials make them ideal for p–i–n device architectures where they serve both as the intrinsic absorption layers and carrier transport layers.[3–6] In a mixed-halide perovskite $CH_3NH_3PbI_{3-x}Cl_x$ system, the presence of a chloride ion source in the precursor solutions results in a strong increase in the overall charge diffusion length, making it particularly suitable for PH configuration. The recent breakthrough of organometal halide perovskite based PH PVK SCs presented a power conversion efficiency (PCE) of 19.3%, which suggests the enormous potential of PH PVK SCs in terms of achieving widely commercial applications.[7]

Currently, there are two main challenges encountered in the fabrication of single solution-processed perovskite films, controlling the crystallization process and ensuring high quality film. Generally, the fast crystallization of perovskite materials with solvent evaporation may result in uncontrollable film morphology. Pinhole formation, poor coverage of the perovskite film, may cause low-resistance shunting paths and lost light absorption, thus poor performance, especially for the PH solar cells.[8] Even though the perovskite film morphology has been investigated as a function of parameters such as the initial precursor concentration, the kinds of solvents used, the solvent evaporation rate, and the time and temperature of annealing, wide morphological variation has resulted in significant differences in the photovoltaic performance, regardless of differences in the fabrication method and device configuration.[9–11] Actually, for the mesoporous structure the high coverage films do not seem to be a mandatory requirement for high performance.[12] However, it is proposed that high perovskite film coverage on compact TiO_2 is the optimum configuration for high performance in the PH architecture. H.J. Snaith *et al.* have pointed out the dependence of perovskite coverage on a wide range of annealing temperature from 90–170 °C and the relationship

Department of Microelectronic Science and Engineering, Ningbo Collaborative Innovation Center of Nonlinear Hazard System of Ocean and Atmosphere, Ningbo University, Ningbo, 315211, China. E-mail: huziyang@nbu.edu.cn, zhuyuejin@nbu.edu.cn; Fax: +86 574 87600744; Tel: +86 574 87600770

† Electronic supplementary information (ESI) available. See DOI: 10.1039/c5cp03934g

between perovskite coverage and device performance in PH PVK SCs.[8] However, considering sufficient coverage of the surface, it is extremely sensitive to the range of annealing temperature and duration during the good crystallization of the perovskite film. The coverage of perovskite film and the electronic structure of perovskite crystals also effect the charge transport and thus the photovoltaic performance.[11–14]

Here, by deliberately controlling the annealing temperature (<100 °C) and duration, $CH_3NH_3PbI_{3-x}Cl_x$ film with coverage approaching 100% and with highly oriented crystal domains results in reproducible and efficient PH PVK SCs. The high coverage of perovskite film ensures adequate absorption and avoids possible short circuit. The highly oriented crystal domains are believed to promote the efficient transport of electrons and holes to their corresponding electrodes, and PH PVK SCs with an average efficiency of 12% and a maximum efficiency of over 15% were achieved.

Results and discussion

PH PVK SCs were fabricated with a structure of fluorine doped tin oxide (FTO)/compact TiO_2 (c-TiO_2)/$CH_3NH_3PbI_{3-x}Cl_x$/spiro-MeOTAD/Ag. The single-step solution-processing method was used to deposit the perovskite films. The perovskite films were treated by time–temperature dependent annealing (TTD) from 60 °C to 95 °C as shown schematically in Fig. 1(a). To investigate the effect of the annealing temperature and duration on perovskite film composition and morphology and to characterize the perovskite films formed, we employed X-ray diffraction (XRD), ultraviolet-visible absorption spectroscopy (UV-vis), scanning electron microscopy (SEM) and atomic force microscopy (AFM) measurements. XRD measurements were conducted to investigate the nature of the material formed by following the above annealing process. Normally, low annealing temperatures result in an incomplete conversion to the perovskite. The XRD diffractograms for samples annealed at 80 °C/35 min exhibit typical peaks that are mainly attributed to the precursor materials. By simply drying the films, the excess solvent is removed, while the precursor solution is insufficient to convert into the desired perovskite film, as indicated by the presence of strong lead chloride ($PbCl_2$) XRD diffraction peaks in Fig. 1(b). Apart from the $PbCl_2$ peaks there are several peaks that remain unidentified, which may be attributed to the possible formation of byproducts such as lead(II) oxychloride.[12] Upon increasing the annealing temperature to 85 °C/55 min, we can see that some of the diffraction peaks disappeared; meanwhile the color of the film turned similar to that of the just spin-coated film (Fig. S1(d), ESI†). The specific mechanism of this phenomenon related to the evolution of intermediates is unclear at present. The evolved color of the perovskite films is shown in Fig. S1 (ESI†). When the temperature reached 95 °C/65 min, a set of new peaks appeared (indicated by #), matching those reported for the $CH_3NH_3PbI_3$ crystallized in the tetragonal perovskite structure.[3,5,6] The peaks at 14.2°, 28.5°, 43.3°, and 59.0° are correspondingly assigned to the (110), (220), (330) and (440) planes, respectively. Though the diffraction peaks of lead chloride are weak, we still speculate that the conversion from precursor materials to perovskite structure is incomplete at this stage. Upon continuing annealing at 95 °C/75–115 min, it is found that the position of perovskite diffraction peaks remains unchanged, while the intensity of diffraction peaks changes slightly. This phenomenon confirms that the crystal structure of perovskite is stably developed under this annealing condition.

The corresponding UV-visible absorption spectrum change of perovskite films (Fig. 1(c)) is consistent with that of XRD during the growth of perovskite films. At 80 °C/35 min, no absorption peak that belongs to the perovskite can be found, suggesting that the precursor has not yet begun to react at this time. From 85 °C/55 min to 95 °C/65 min, the absorption peak at 760 nm corresponding to the direct band gap transition from the first valance band to the conduction band gradually emerged, implying that the perovskite growth started at this stage. At the same time, we observed that the color of the film changed gradually from pale yellow to reddish brown during this period. Therefore, we suggest that a temperature of ~95 °C is critical for the perovskite growth. Upon continuing annealing at 95 °C, the absorption spectrum shape of the film was found to be almost the same except for a subtle change in the absorption intensity over each wavelength range, which also indicates the gradual development of perovskite crystals. By deliberately controlling the annealing temperature and duration, no presence of lead iodide (PbI_2) or lead chloride ($PbCl_2$) was found in the final perovskite film. So we assume that the perovskite films well evolved into perfect crystals. However, the previous results reported that traces of PbI_2 or $PbCl_2$ existed

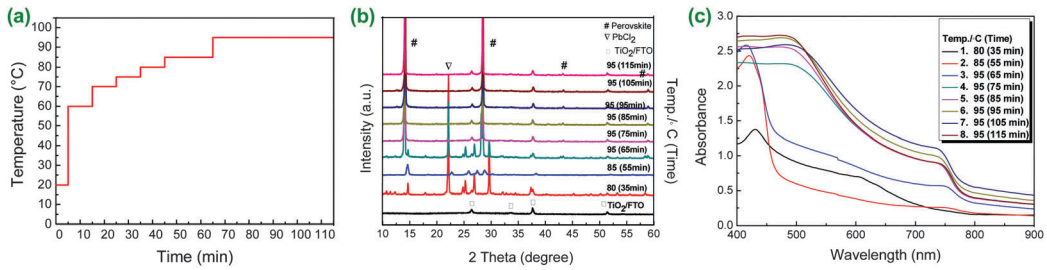

Fig. 1 (a) Schematic diagram of the thermal annealing method under time–temperature dependent treatment for perovskite films, (b) X-ray diffraction patterns of compact TiO_2 films with perovskite films annealed at different stages under time-dependent temperature, (c) UV-vis absorption spectra for compact TiO_2 films with perovskite films annealed at different time periods.

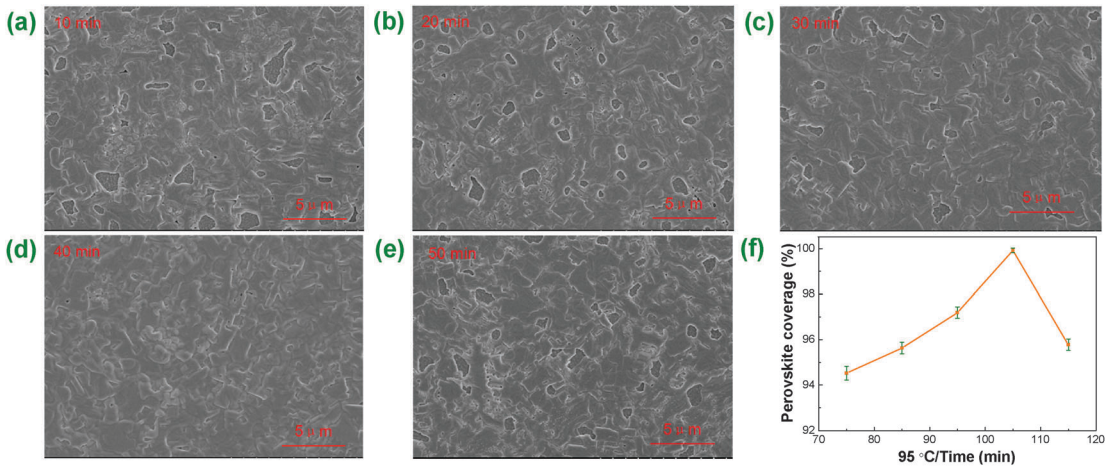

Fig. 2 SEM images of compact TiO_2 films with perovskite films annealed at 95 °C for different time periods and the corresponding surface coverage as a function of annealing time.

in the perovskite film even after the film was well crystallized, and the existing PbI_2 or $PbCl_2$ was beneficial for electron transportation.[15,16]

The influence of the annealing temperature on the morphology of the perovskite films was examined by SEM. We mainly focus on the evolution of perovskite crystal structure and morphology, annealing under different conditions to optimize the perovskite morphology, and are little concerned about the process of transition from precursor to perovskite. Since the perovskite was well crystallized at 95 °C as we discussed above, here we only concentrate on examining the perovskite film annealed at this temperature for different periods of time. Fig. 2 shows the SEM images of representative perovskite films annealed at 95 °C for different periods of time. The calculated coverages plotted in Fig. 2(f) were estimated from SEM images by using the threshold function in the ImageJ program, simply by setting a threshold on the image and calculating the area above and below the threshold.[17] In perovskite films annealed at 95 °C for 10 min, many pores of rather large size can be found (Fig. 2(a)). As annealing time increases, the total number of pores in the final film decreases, meanwhile the distribution of their pore size tends to a narrow range. The film annealed at 95 °C for 40 min has an excellent coverage approaching 100%, as few pinholes can be found (Fig. 2(d)). Upon increasing the annealing time further (>50 min), some pinholes and small particles appeared, thus decreasing the coverage (Fig. 2(e)). Crystal growth is a very complex process that involves a variety of thermodynamics and energetic processes. It is proposed that non-uniform temperature leads to non-uniform grain size and thus to the presence of micro-holes inside the crystal; rapid heating could be one cause of non-uniform temperature. For perovskite films, slow and low heating is potentially necessary for crystal growth with few grain boundaries, microvoids, pinholes and little internal stress. We obtained perovskite films with coverage approaching 100% and with highly oriented crystal domains through appropriate control of the annealing temperature and duration. Here, combining this knowledge with our results, we propose that the annealing temperature and time of 95 °C/40 min is ideal to obtain perovskite film with a maximum coverage.

Supposing that the pinholes were uncovered by the perovskite film, we calculated the surface coverage of perovskite films. It is needed to clarify whether those areas in pinholes are really exposed c-TiO_2 or concealed c-TiO_2 covered by very thin perovskite film. To this end, we selected a visually better coverage perovskite sample (annealed at 95 °C for 30 min) for characterization by SEM associated with energy-dispersive X-ray spectroscopy (EDX). Compared to the only c-TiO_2 layer spin-coated on the FTO substrate shown in Fig. 3(b), some isolated island particles of size ranging from 50 to 100 nm on top of the c-TiO_2 layer can be seen in Fig. 3(a), which we believe are perovskite nanocrystalline. In order to confirm the validity of this conjecture, we examined a representative pinhole and its adjacent areas by EDX. The scanning direction is along the white line from the left to the right as shown in Fig. 3(c). As elements with relatively small atomic weight such as hydrogen, carbon, and nitrogen are not easily detectable, only heavy elements such as lead, iodine, and chlorine were obviously detected in the test. EDX spectra showed that lead, iodine, and chlorine contents decreased significantly in the "pinhole" area, but did not tend to zero. Also, we noticed a slight reduction in the carbon content, one of the constituent elements of perovskite (indicated by the red curve), in the pinhole as shown in Fig. 3(c), and careful examination shows that the carbon content in the pinhole is not zero. Therefore, we believe that the island-shaped particles in the "pinhole" area should be perovskite but not $PbCl_2$ or PbI_2.

On the other hand, AFM characterization shows that the average depth of the pinholes is about 300 nm (Fig. S2, ESI†), considered together with the 350–400 nm thickness of the perovskite film extracted from the cross-sectional SEM image (Fig. S3, ESI†) of the device; we can determine that the thickness of the discontinuous perovskite film in the pinhole is in the range of 50–100 nm, which is consistent with the above-described particle size observed by SEM. Therefore, we believe that the island-like particle in the "pinhole" area is a thin perovskite

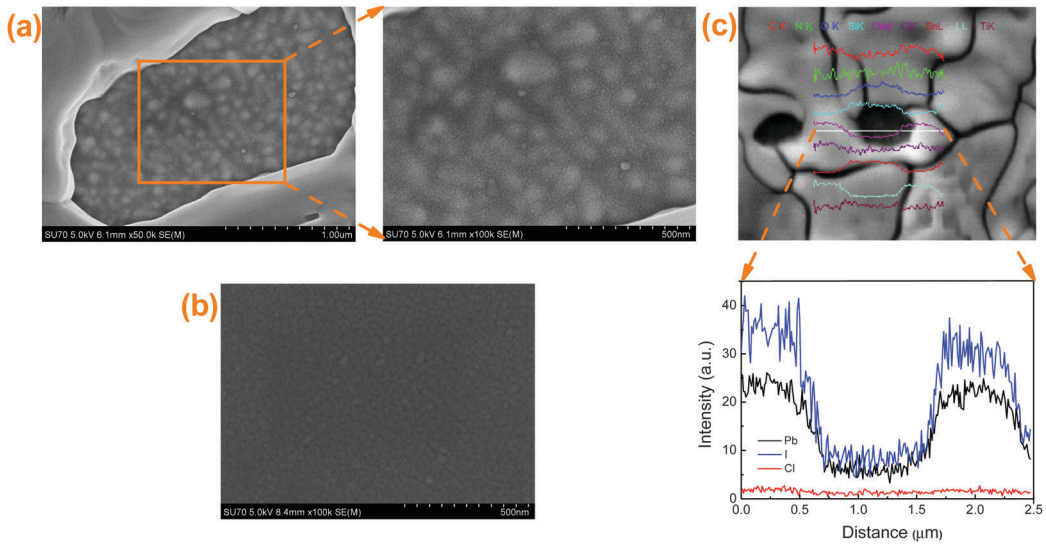

Fig. 3 (a) SEM images of a pinhole of perovskite film on the compact TiO_2/FTO glass substrate and (b) the compact TiO_2 layer on the FTO glass substrate, (c) energy-dispersive X-ray spectroscopy of a pinhole and its adjacent areas; the scanning direction is along the white line shown from the left to the right.

nanocrystalline film (50–100 nm). As for the specific formation mechanisms of these pinholes, more studies to further optimize the growth of the perovskite film are urgently needed. With the combination of encouraging characteristics including nearly full surface coverage, large grain size, and a high degree of crystallization, we can expect promising photovoltaic performance by annealing at appropriate temperature. The photovoltaic performance of PH SCs was examined and the current–voltage (J–V) characteristics were determined under standard AM 1.5G illumination. All the performance parameters are summarized in Table 1. We can find that the device with the ideal perovskite film annealed gives the highest PCE of 15.17%, as a result of the highest open-circuit voltage (V_{OC}), fill factor (FF) and short current density (J_{SC}), 1.02 V, 21.65 mA cm^{-2} and 67.54%, respectively. The corresponding J–V characteristics and incident photo-current conversion efficiency (IPCE) spectra are shown in Fig. 4(b and c), respectively. The calculated integrated J_{SC} value (20.92 mA cm^{-2}) based on the IPCE curve is very consistent with the J_{SC} value (21.65 mA cm^{-2}) obtained from the J–V curve recorded under a 100 mW cm^{-2} solar simulator, as shown in Fig. 4(c). It should be noted that the observed and calculated J_{SC} values show negligible mismatch. It is obvious that the device with perovskite film has a coverage of nearly 100% and thus shows the best performance. Histograms of device efficiency (Fig. 4(d)) measured for 40 separate PVK SCs show that the annealing treatment scheme mentioned above can enable achieving reproducible efficient PH PVK SCs without any further, more complex modification.

Table 1 Photovoltaic performance parameters extracted from J–V measurements under standard AM 1.5G illumination of devices with perovskite films annealed at 95 °C for different time periods

Annealing time (min)	V_{OC} (V)	J_{SC} (mA cm^{-2})	FF (%)	PCE (%)	Coverage (%)
10	0.917	19.35	60.34	10.89	94.53 ± 0.30
20	0.932	20.47	59.14	11.48	95.63 ± 0.25
30	0.931	21.55	59.19	12.08	97.19 ± 0.25
40	1.02	21.65	67.54	15.17	99.85 ± 0.10
50	0.974	19.71	65.41	12.77	95.78 ± 0.25

We now discuss the relationship between device performance parameters and coverage of the perovskite films. As shown in Table 1, J_{SC} shows a clear trend with coverage. At a coverage of 94.53%, J_{SC} is ~19.4 mA cm^{-2}. As the coverage increases up to 97.19%, J_{SC} increases linearly, up to ~21.6 mA cm^{-2}. After that, J_{SC} increases very slowly with coverage, up to 21.65 mA cm^{-2}. The device V_{OC} and FF also improve with increasing coverage, the device with the highest coverage presents the best V_{OC} and FF. For efficient PH PVK SCs, a highly uniform, pinhole-free and high surface coverage perovskite film is extremely significant, as also required in other thin film solar cells.[10,14] The films produced by the conventional spin-coating and annealing method contain larger and rod-like grains with an incomplete coverage on the substrate, as reported in previous observations.[6] A poor coverage not only allows the light to pass straightly through without absorption but also results in a high frequency of "shunt paths" that leads to a direct contact between spiro-OMeTAD and the c-TiO_2 layer. Hence we still believe that high coverage is a necessary prerequisite for high device performance.

In addition to high coverage, we believe that there are other factors contributing to the high efficiency as described below. The SEM image (Fig. 5(a)) shows that the perovskite film grown at 95 °C for 40 min contains columnar crystals, whose top and bottom surfaces are parallel to the electrode plane. Furthermore, XRD analysis (Fig. 5(b)) shows that the resulting perovskite films onto the substrate have highly oriented crystal domains with the long c-axis preferentially oriented parallel to the substrate as the (110), (220), (330), (440) reflections are indicated.[3,4,18] Here, anisotropic electron transport properties of the perovskite

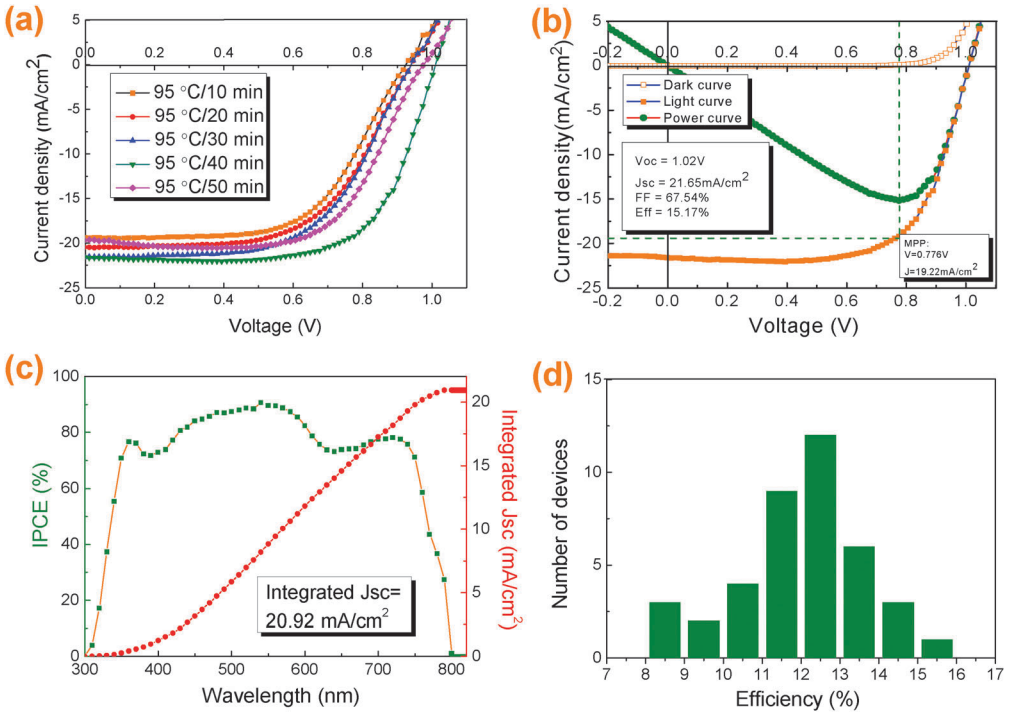

Fig. 4 (a) Current–voltage characteristics of the corresponding devices with the perovskite films annealed at 95 °C for different time periods, (b) current–voltage curves of the best solar cell, (c) the corresponding incident photo-current conversion efficiency spectra, (d) histograms of device efficiency measured for 40 separate perovskite solar cells.

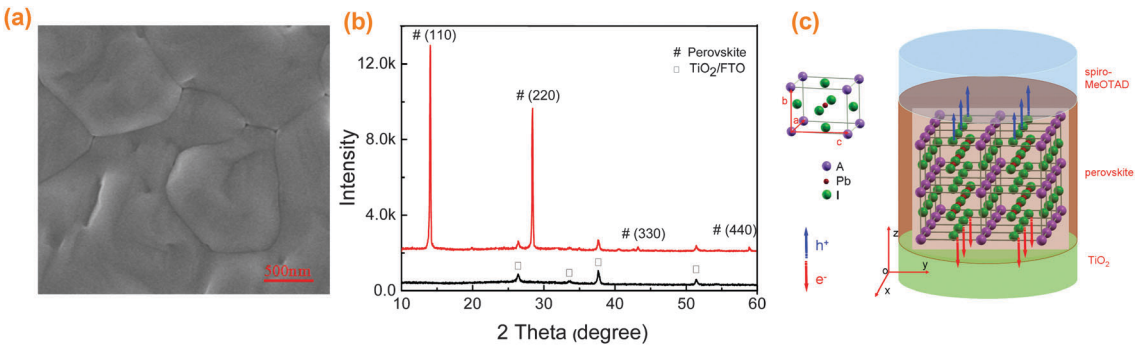

Fig. 5 (a) Top view SEM image of perovskite film annealed at 95 °C for 40 min, (b) XRD measurement of perovskite film annealed at 95 °C for 40 min, (c) the schematic diagram of the anisotropic electron transport properties of perovskite crystal, A is methylammonium.

crystals may contribute to a large J_{SC}.[18] As shown in Fig. 5(c), the XOY represents the plane of the substrate which is parallel to the TiO_2 electron transport layer and the spiro-MeOTAD hole transport layer. The vertical axis, OZ, represents the direction perpendicular to the substrate. It is well known that, in the perovskite crystal, the layered organic cation and inorganic lead halide ions are alternately stacked, thus constructing a three-dimensional structure. The simple organic layers consisting of a short-chain of organic cations help to define the degree of interaction and the properties arising in the inorganic layers. A long-chained, ordered PbI_6 octahedral system is actually very beneficial for electron transport, endowing the perovskite material with excellent electron transport properties.[19,20] In our case, the perovskite films have highly oriented crystal domains with the long *c*-axis preferentially oriented parallel to the substrate. This kind of crystal domain orientation ensures that there exist countless planes of PbI_6 octahedra perpendicular to the electrodes. Due to the excellent electron transport properties of the PbI_6 octahedral plane, electrons and holes can be efficiently transported in the vertical direction across the device, and finally collected by the cathode and anode, respectively. The anisotropic charge transport properties of the perovskite crystals contribute to the increased J_{SC}, improved FF and thus the improved PCE. The totally low FF of the devices ($<70\%$) is attributed to the mismatch of the poor conductivity of the undoped c-TiO_2 electron transport layer and the high conductivity of the spiro-MeOTAD hole transport layer with high concentration doping.[21] To further increase the overall performance of the

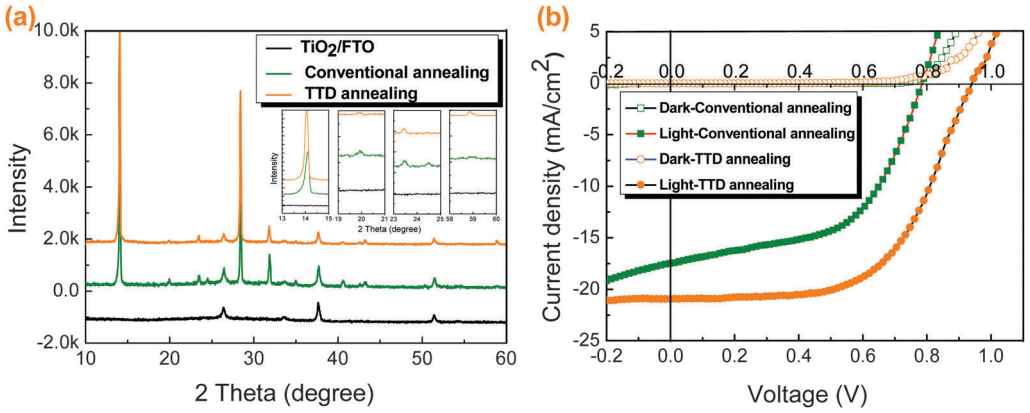

Fig. 6 (a) XRD patterns for perovskite films annealed with different methods (the inset gives the detailed comparison of diffraction intensity) and (b) the *J–V* curves of their corresponding devices.

device, using doped c-TiO_2 as the electron transport layer may be considered.[22]

The perovskite films have highly oriented crystal domains with the long *c*-axis preferentially oriented parallel to the substrate, which is beneficial for anisotropic charge carrier transport. To confirm the validity of the above hypothesis for an anisotropic electron transport model, we further compared the XRD patterns of perovskite films and the performance of corresponding devices that were prepared using the conventional annealing method and our optimized annealing method (TTD annealing). Fig. 6(a and b) shows the XRD patterns of perovskite films that were treated by two different annealing methods and the *J–V* curves of corresponding devices. Fig. 6(a) reveals that the intensity of the diffraction peaks at around 14.2°, 28.5°, 43.3°, and 59.0°, which are assigned to the (110), (220), (330), and (440) lattice planes of the tetragonal perovskite structured $CH_3NH_3PbI_3$ crystals, of the perovskite film treated by the conventional annealing method is weaker than that of the perovskite film treated by the TTD annealing method. Besides that, with regard to the perovskite film that was treated by the conventional annealing method some new peaks at around 20.0°, 24.0°, 24.5°, which should be assigned to the other lattice planes of the tetragonal perovskite structured $CH_3NH_3PbI_3$ crystals, were observed. All these observed facts reveal that the optimized perovskite thin film prepared by the TTD annealing method has better crystal orientation with the long *c*-axis preferentially oriented parallel to the substrate. Fig. 6(b) gives the *J–V* curves of the corresponding devices which reveal that the device with the perovskite films treated by the TTD annealing method surpasses that with the perovskite films treated by the conventional annealing method in terms of photovoltaic performance. This result suggests that anisotropic electronic properties of the perovskite crystals may have a great influence on the performance of the device.

Fig. 7 presents the plan view SEM images (a and b) of the perovskite films annealed with different methods and the cross-sectional SEM images (c and d) of their corresponding devices. The perovskite film treated by the conventional annealing method shows large pinholes and surface defects, judging from

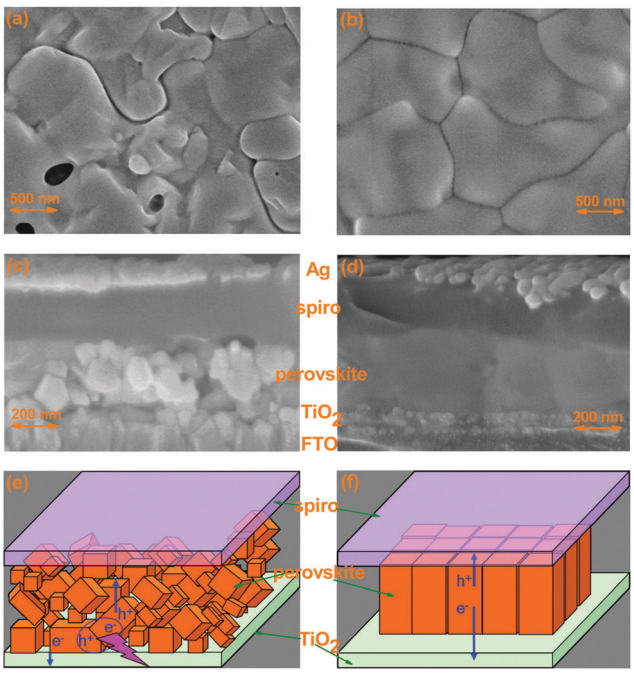

Fig. 7 (a and b) Plan view SEM images of the perovskite films annealed with different methods and (c and d) cross-sectional SEM images of their corresponding devices. (e and f) Charge transport model of the corresponding devices. (a, c and e) Correspond to the conventional annealing method and (b, d and f) correspond to the TTD annealing method.

the crystal particle sizes and film morphology (Fig. 7(a)), while the perovskite film treated by the TTD annealing method was more compact and uniform (Fig. 7(b)). This is also consistent with the XRD patterns with different diffraction intensity. The cross-sectional SEM images of the device treated by the conventional annealing method (Fig. 7(c)) shows that the porous perovskite film contains irregular perovskite crystals of small sizes (~100 to 200 nm) with inevitable pores. Obviously, these pores are unfavorable for light absorption and charge transport along the film thickness direction. Specifically, such a perovskite film is actually made up of several layers of stacked grains, and this can result in many grain boundaries parallel to the substrate

which can be charge recombination centers on the path of charge transport (Fig. 7(e)). The perovskite film treated by the TTD annealing method (Fig. 7(d)) was composed of densely packed perovskite grains whose sizes are comparable to the thickness of the film and no grain boundaries were found to be parallel to the substrate. So the perovskite film in fact consists of a monolayer of single crystalline grains. Thus the photogenerated charges at any spatial point of the perovskite film can transport within the densely packed columnar crystals and will not encounter grain boundaries that can easily induce charge recombination before transporting to the corresponding electrodes (Fig. 7(f)). Therefore, efficient electron and hole transport and collection with reduced energy loss resulted in high performance. Here, it should be emphasized that the anisotropic electron transport originates from highly oriented crystal domains and the densely packed columnar crystals are simultaneously needed for efficient charge transport and high device performance.

Finally, we discuss the hysteresis effect on the *J–V* measurement of the device and the device stability; the results are shown in Fig. S4 (ESI†). For the *J–V* measurement a scanning speed of 0.03 V s^{-1} is adopted both for forward and reverse scan. As shown in Fig. S4(a) (ESI†), the red and green lines represent data measured with reverse scan and forward scan, respectively, where reverse scan defines a measure from open-circuit to short-circuit and forward scan is *vice versa*. The device showed an obvious hysteresis effect which needs further interface modification. We attribute the anomalous hysteresis to the poor electronic contact existing between the perovskite and the charge collection layer.[23] For stability investigation, the tested device without encapsulation was stored in a glove box full of dry nitrogen, and taken outside and tested every 1 day for 7 days. As shown in Fig. S4(b) (ESI†) the device retains 60–65% of the initial performance after 3 days, and 40–45% after 7 days, respectively. In order to further promote the practical application of perovskite solar cells, appropriate encapsulation is urgently needed.

Conclusions

In summary, we have demonstrated an effective growth method to fabricate perovskite films with coverage approaching 100% by carefully controlling the annealing temperature and duration. A combination of SEM, XRD, and AFM indicated that the as-prepared perovskite film exhibits highly uniform and oriented crystal domains. Highly reproducible PCEs of PVK SCs with an average value of 12% and a maximum value of 15.17% were achieved in the PH structure. Anisotropic electron transport properties of the perovskite crystals have been proposed to explain the observed photovoltaic performance. The monolayer perovskite film of columnar crystals with highly oriented crystal domains is demonstrated to be an ideal structure for the PH PVKSC, device which would facilitate fast charge transport. Higher reproducible performance could be expected for PH PVK SCs with optimization of the other functional layer based on this perovskite film growth method.

Experimental procedures

Materials

All the chemicals were used as received, including $PbCl_2$ (99.999%, Sigma-Aldrich), CH_3NH_3I (Materwin, Shanghai), $TiCl_4$ (Sigma-Aldrich), titanium(IV) isopropoxide (98+%, Acros), diethanolamine (98%, Sigma-Aldrich), spiro-OMeTAD (Lumtec), dimethylformamide (DMF), Li-bis (trifluoromethanesulfonyl) imide (Li-TFSI, Acros), 4-*tert*-butylpyridine (Sigma-Aldrich), acetonitrile, ethanol, and chlorobenzene.

Device fabrication

First, hydrochloric acid etched, FTO-coated glass substrates (Nippon, 14 Ω □$^{-1}$) were cleaned by ultrasonication in an alkaline, aqueous washing solution, rinsed with deionized water, ethanol and acetone, and subjected to an ozone-ultraviolet treatment for 15 min. An ~40 nm thick TiO_2 compact layer was then deposited on the substrates by spin-coating using a titanium diisopropoxide bis(acetylacetonate) sol–gel solution. The sol-gel solution was spin-coated on the substrates at 4000 rpm for 25 s, followed by annealing at 120 °C for 15 min and then 450 °C for 1 h. After cooling to room temperature, the substrates were treated in a 0.04 M aqueous solution of $TiCl_4$ for 30 min at 70 °C, rinsed with deionized water and dried at 120 °C for 15 min.

For the perovskite layer, a 1 : 3 ratio of $PbCl_2$/CH_3NH_3I was mixed in DMF. Specifically, the concentration of the $PbCl_2$ and CH_3NH_3I were 0.73 and 2.2 M. The mixture solution was stirred at 60 °C overnight and spin-coated on the FTO/c-TiO_2 substrates at 2000 rpm for 40–50 s. The single-step solution-processing method was used to deposit the perovskite films. The time–temperature dependent annealing treatment is illustrated in Fig. 1(a). A transparent yellowish film forms naturally once deposition of the precursor solution on the FTO/c-TiO_2 substrate is complete. Upon leaving the film at room temperature for several minutes, the color of the film changes to red, then becomes deep yellow and finally deep black. The final perovskite film was formed by annealing from 60 °C to 95 °C for different periods of time. In the conventional annealing method, the FTO/c-TiO_2 substrates with as-spin-coated perovskite precursor layers were annealed at 100 °C for 45 min.

After the deposition of perovskite materials, a hole transport layer (HTL) solution was spin-coated at 2800 rpm for 30 s, where 1 mL spiro-OMeTAD/chlorobenzene (72.3 mg mL^{-1}) solution was employed with addition of 18 μL Li-TFSI/acetonitrile (520 mg mL^{-1}), and 29 μL 4-*tert*-butylpyridine. Finally, a 120 nm thick silver layer was thermally evaporated on top of the device under a pressure of 5×10^{-6} Torr to form the back contact. The as-fabricated device consists of a 450 nm thick FTO electrode, 40 nm of TiO_2, 400 nm of perovskite, 400 nm of spiro-MeOTAD, and 120 nm of Ag.

Characterizations

X-ray diffraction patterns (2θ scans) were obtained from samples of perovskite deposited on the FTO/c-TiO_2 substrates using an X-ray diffractometer (XRD, D8 Advance, Bruker AXS, Germany), using Cu-Kα radiation (λ = 1.54050 Å). The UV–visible absorption spectra of the perovskite films were recorded with a Cary 5000

UV-vis-NIR spectrophotometer. A scanning electron microscope (SEM, Hitachi SU-70, Japan) was used for recording the SEM images. Atomic force microscopy (AFM) was performed using a Bruker Dimension 5000 Scanning Probe Microscope (SPM) in ''tapping mode''.

The current density–voltage (J–V) curve measurements were conducted with an AM 1.5 solar simulator equipped with a 1000 W xenon light source and an AM 1.5G type filter (Newport, 81904, USA). The light intensity of the solar simulator was adjusted by using a standard Si cell. J–V curves were obtained by applying an external bias to the cell, and measurements were recorded with a Keithley model 2400 digital source meter. The effective area of the cell was defined to be 0.04 cm^2 using a nonreflective metal mask.

The incident photo-current conversion efficiency (IPCE) spectra were measured in air on a Newport 2936-c power meter under the irradiation of a 300 W xenon light source with an Oriel Cornerstone 260 1/4 monochromator in DC mode. A reference scan with the Si detector was taken prior to the sample measurement, to allow the background to be subtracted.

Acknowledgements

This work was supported by the National Science Foundation of China (Grant No. 11374168, 11304170, 51302137), the Natural Science Foundation of Zhejiang Province (Grant No. LQ13F050007), and the Foundation of Zhejiang Educational Commission (Grant No. Y201326905). The authors would like to thank the sponsor by K.C. Wong Magna Fund in Ningbo University.

Notes and references

1 S. D. Stranks, G. E. Eperon, G. Grancini, C. Menelaou, M. J. P. Alcocer, T. Leijtens, L. M. Herz, A. Petrozza and H. J. Snaith, *Science*, 2013, **342**, 341–344.
2 G. C. Xing, N. Mathews, S. Y. Sun, S. S. Lim, Y. M. Lam, M. Gratzel, S. Mhaisalkar and T. C. Sum, *Science*, 2013, **342**, 344–347.
3 A. Kojima, K. Teshima, Y. Shirai and T. Miyasaka, *J. Am. Chem. Soc.*, 2009, **131**, 6050.
4 M. M. Lee, J. Teuscher, T. Miyasaka, T. N. Murakami and H. J. Snaith, *Science*, 2012, **338**, 643.
5 M. Z. Liu, M. B. Johnston and H. J. Snaith, *Nature*, 2013, **501**, 395–398.
6 J. Burschka, N. Pellet, S. J. Moon, R. Humphry-Baker, P. Gao, M. K. Nazeeruddin and M. Gratzel, *Nature*, 2013, **499**, 316–320.
7 H. P. Zhou, Q. Chen, G. Li, S. Luo, T. B. Song, H. S. Duan, Z. R. Hong, J. B. You, Y. S. Liu and Y. Yang, *Science*, 2014, **345**, 542–546.
8 G. E. Eperon, V. M. Burlakov, P. Docampo, A. Goriely and H. J. Snaith, *Adv. Funct. Mater.*, 2014, **24**, 151–157.
9 Q. Chen, H. P. Zhou, Z. R. Hong, S. Luo, H. S. Duan, H. H. Wang, Y. S. Liu, G. Li and Y. Yang, *J. Am. Chem. Soc.*, 2013, **136**, 622–625.
10 M. Saliba, K. W. Tan, H. Sai, D. T. Moore, T. Scott, W. Zhang, L. A. Estroff, U. Wiesner and H. J. Snaith, *J. Phys. Chem. C*, 2014, **118**, 17171–17177.
11 R. Kang, J. E. Kim, J. S. Yeo, S. Lee, Y. J. Jeon and D. Y. Kim, *J. Phys. Chem. C*, 2014, **118**, 26513–26520.
12 A. Dualeh, N. Tétreault, T. Moehl, P. Gao, M. K. Nazeeruddin and M. Grätzel, *Adv. Funct. Mater.*, 2014, **24**, 3250.
13 Y. Z. Wu, A. Islam, X. D. Yang, C. J. Qin, J. Liu, K. Zhang, W. Q. Peng and L. Y. Han, *Energy Environ. Sci.*, 2014, **7**, 2934–2938.
14 M. Xiao, F. Huang, W. Huang, Y. Dkhissi, Y. Zhu, J. Etheridge, A. Gray-Weale, U. Bach, Y. B. Cheng and L. Spiccia, *Angew. Chem., Int. Ed.*, 2014, **126**, 10056.
15 D. H. Cao, C. C. Stoumpos, C. D. Malliakas, M. J. Katz, O. K. Farha, J. T. Hupp and M. G. Kanatzidis, *APL Mater.*, 2014, **2**, 091101.
16 N. Li, H. P. Dong, H. Dong, J. L. Li, W. Z. Li, G. D. Niu, X. D. Guo, Z. X. Wu and L. D. Wang, *J. Mater. Chem. A*, 2014, **2**, 14973.
17 W. Rasband, ImageJ 2005, http://rsb.info.nih.gov/ij/, accessed: November 2014.
18 P. Docampo, F. C. Hanusch, N. Giesbrecht, P. Angloher, A. Ivanova and T. Bein, *APL Mater.*, 2014, **2**, 081508.
19 D. B. Mitzi, K. Chondroudis and C. R. Kagan, *IBM J. Res. Dev.*, 2001, **45**, 29–45.
20 T. Baikie, Y. N. Fang, J. M. Kadro, M. Schreyer, F. X. Wei, S. G. Mhaisalkar, M. Graetzel and T. J. White, *J. Mater. Chem. A*, 2013, **1**, 5628.
21 J. H. Noh, N. J. Jeon, Y. C. Choi, M. K. Nazeeruddin, M. Gratzel and S. Seok, *J. Mater. Chem. A*, 2013, **1**, 11842.
22 K. Manseki, T. Ikeya, A. Tamura, T. Ban, T. Sugiura and T. Yoshida, *RSC Adv.*, 2014, **4**, 9652.
23 C. Tao, S. Neutzner, L. Colella, S. Marras, A. R. Srimath Kandada, M. gandini, M. De Bastiani, G. Pace, L. Manna, M. Caironi, C. Bertarelli and A. Petrozza, *Energy Environ. Sci.*, 2015, **8**, 2365–2370.

